nature materials

ARTICLES

PUBLISHED ONLINE: 16 JANUARY 2011 | DOI: 10.1038/NMAT2941

Experimental analysis of charge redistribution due to chemical bonding by high-resolution transmission electron microscopy

Jannik C. Meyer[1]*†, Simon Kurasch[1], Hye Jin Park[2], Viera Skakalova[2], Daniela Künzel[3], Axel Groß[3], Andrey Chuvilin[1,4], Gerardo Algara-Siller[1,5], Siegmar Roth[2,6], Takayuki Iwasaki[2], Ulrich Starke[2], Jurgen H. Smet[2] and Ute Kaiser[1]*

The electronic charge density distribution or the electrostatic atomic potential of a solid or molecule contains information not only on the atomic structure, but also on the electronic properties, such as the nature of the chemical bonds or the degree of ionization of atoms. However, the redistribution of charge due to chemical bonding is small compared with the total charge density, and therefore difficult to measure. Here, we demonstrate an experimental analysis of charge redistribution due to chemical bonding by means of high-resolution transmission electron microscopy (HRTEM). We analyse charge transfer on the single-atom level for nitrogen-substitution point defects in graphene, and confirm the ionicity of single-layer hexagonal boron nitride. Our combination of HRTEM experiments and first-principles electronic structure calculations opens a new way to investigate electronic configurations of point defects, other non-periodic arrangements or nanoscale objects that cannot be studied by an electron or X-ray diffraction analysis.

The redistribution of charge that occurs when free atoms are arranged into a solid or molecule is of tremendous interest. It is the distribution of the binding electrons and their energy levels that defines, to a large extent, the properties of a material. According to the Hohenberg–Kohn theorem[1,2], all ground-state electronic properties can be derived from the electronic charge density distribution; this theorem is also the basis for the density functional theory (DFT) approach to first-principles electronic structure calculations. The interatomic electrostatic potential is directly related to the charge distribution through Poisson's equation, and hence, provides equivalent information. Charge density or electrostatic potential can be directly probed by the scattering of X-rays or electrons, respectively. However, a high precision is needed to obtain information that goes beyond the structure of the compound, so far obtained only from X-ray[3,4] or electron diffraction[5,6] experiments. Measurements of electronic charge densities can be used to reveal the nature of chemical bonds[3] or to determine the ionicity of atoms in a compound[6]. Moreover, high-precision experimental data can be used to verify a calculated charge density[7], even if a complete reconstruction is not possible[8]. This is particularly important for complex materials where the modelling, the involved approximations and discretization are not straightforward. For example, important details in the electronic configuration of copper oxide[9] or magnesium diboride[10] have been clarified by the combination of an electron and X-ray diffraction analysis with first-principles calculations.

In spite of these direct methods, most of our knowledge on crystal bonding and electronic structure comes from indirect evidence and theory[6]. One reason is the experimental difficulty to obtain charge density or crystal potential measurements with a sufficiently high accuracy. Moreover, diffraction experiments are limited to sufficiently large periodic structures, and hence, exclude the study of individual interfaces or point defects. In addition, there exist competing spectroscopic techniques that can provide information about the local electronic structure with high spatial resolution[11–17]. For example, atom-resolved electron energy-loss spectroscopy provides not only information about the elemental composition, but also adjustments to the energy levels from the local environment[12–15]. As another example, the combination of scanning tunnelling microscopy and spectroscopy can provide electronic spectra from interfaces or point defects[18–20], but is inherently limited to surfaces.

Here, we show that a charge transfer between neighbouring atoms can be analysed on the basis of atomically resolved HRTEM. The effect of binding electrons on HRTEM image contrast has been explored through calculations in previous studies[21–24], but the effects were not detected experimentally. However, in the same way as in X-ray or electron diffraction experiments, the influence of chemical bonds on HRTEM image contrast becomes discernible and relevant once a sufficient accuracy is obtained in the experiment. We demonstrate this for two cases that would both be inaccessible with a diffraction analysis. As a first example, we analyse the electronic configuration around nitrogen-substitution

[1]Central Facility for Electron Microscopy, Group of Electron Microscopy of Materials Science, University of Ulm, 89081 Ulm, Germany, [2]Max Planck Institute for Solid State Research, Heisenbergstr. 1, 70569 Stuttgart, Germany, [3]Institute of Theoretical Chemistry, University of Ulm, 89069 Ulm, Germany, [4]CIC nanoGUNE Consolider, Av. de Tolosa 76, 20018, San Sebastian, Spain and IKERBASQUE, Basque Foundation for Science, 48011, Bilbao, Spain, [5]Technical University Ilmenau, 98693 Ilmenau, Germany, [6]School of Electrical Engineering, WCU Flexible Nanosystems, Korea University, Seoul 136-713, Korea. †Present address: University of Vienna, Department of Physics, 1090 Vienna, Austria. *e-mail: Jannik.Meyer@univie.ac.at; ute.kaiser@uni-ulm.de.

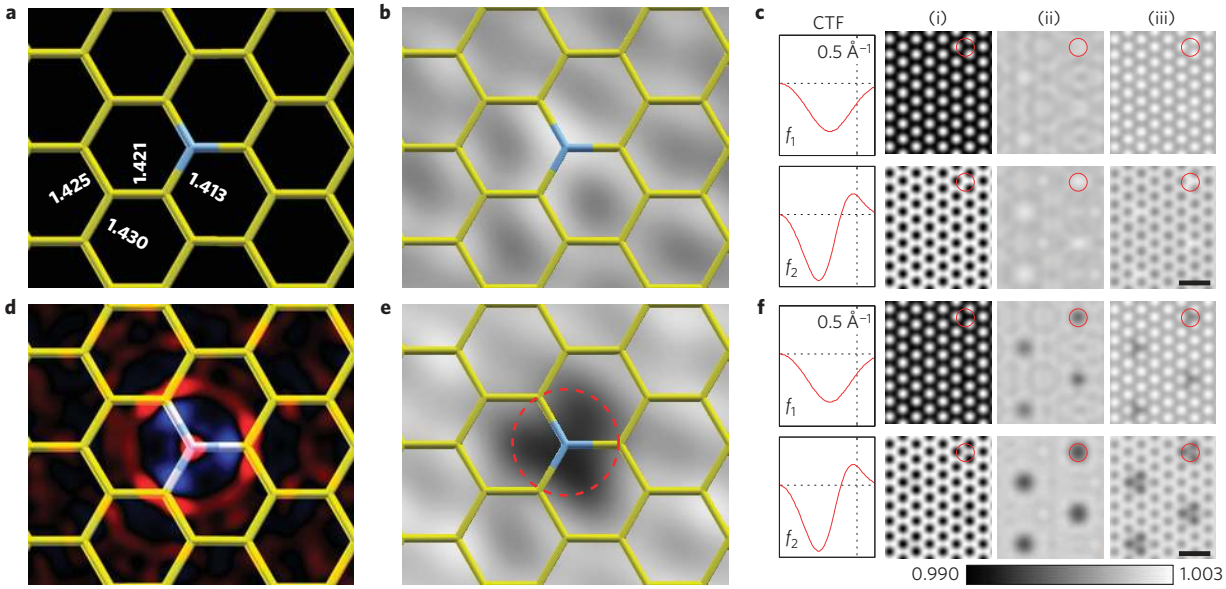

Figure 1 | Charge distribution, projected potentials and TEM simulations for nitrogen-doped graphene. a, Relaxed atomic configuration for a nitrogen substitution in graphene. Bond lengths are given in angstroms. **b**, Projected potential based on the IAM, with the periodic components of the graphene lattice removed, and bandwidth-limited to our experimental resolution (about 1.8 Å). Dark contrast corresponds to higher projected potential values, in accordance with our TEM imaging conditions. **c**, TEM simulation based on the IAM potential, for two experimental conditions (f_1 and f_2, see text). Filters are: (i) unfiltered, (ii) periodic components removed by a Fourier filter, and (iii) low-pass filtered. **d**, Atomic structure (same bond lengths), with the changes in projected electron density due to bonding shown in colour. Blue corresponds to a lower, red to a higher electron density in the DFT result as compared with the neutral-atom (IAM) case. **e**, Projected potential, filtered as in **b**, based on the all-electron DFT calculation. **f**, TEM simulations using the DFT-based potentials. The greyscale calibration bar applies to columns (ii) and (iii), which are all shown on the same greyscale range for direct comparison. The scale bars are 5 Å.

point defects[25] in graphene[26,27]. In this case, we demonstrate that the electronic configuration on the carbon atom next to the nitrogen is perturbed by the defect. In other words, electron scattering on the carbon atom next to the nitrogen is significantly different from electron scattering on a carbon atom elsewhere in the graphene sheet. The second example, hexagonal boron nitride (hBN), is well known to be ionic in the bulk form[28]. We confirm the ionicity for the single-layer hBN structure from HRTEM measurements. Although single-layer hBN is crystalline, experimentally obtained free-standing single-layer hBN samples for HRTEM studies are only a few nanometres in size[29–32], and therefore a diffraction analysis is not practically possible so far. In both cases, the precisely defined sample geometries in terms of thickness (one layer), amorphous adsorbates and defects (none in the selected regions), along with very high sample stability and therefore unprecedented signal-to-noise ratios (by using lower acceleration voltages to avoid sample damage) enable sufficiently accurate measurements. Our analysis on the basis of HRTEM measurements provides a sensitivity to charge transfer on a single-atom level. This opens a new way to study electronic configurations, in particular for point defects, other non-periodic arrangements or nanoscale objects that cannot be analysed in a diffraction experiment.

HRTEM images are conventionally analysed on the basis of the so-called independent atom model[33] (IAM), sometimes also called the procrystal model[10]. In this model, the potential of a solid is calculated as a superposition of atomic potentials that have once been calculated for an isolated atom of every element[34]. This is reasonable as a first approximation because the adjustments to the potentials due to bonding electrons are small. Moreover, the IAM result is useful for comparison, because the effects of chemical bonds can be easily recognized from the difference between the 'real' situation and the IAM approximation[9,10]. Therefore, we will discuss the image simulations based on the IAM, as well as image simulation based on more accurate potentials from DFT calculations in comparison. Both, HRTEM experiments and first-principles electronic structure calculations, show that the IAM is not sufficient for accurate transmission electron microscopy (TEM) image simulations of our example materials.

We begin our results and discussion with the case of nitrogen-doped graphene. The atomic configuration has been considered in many previous works (for example, refs 35,36), and it was found that the C–N bond length in this configuration is nearly identical to the C–C bond length in graphene (with differences less than 2 pm, Fig. 1a). Then, on the basis of neutral, isolated-atom (IAM) scattering factors, one would not expect that a nitrogen substitution in graphene can be detected at all. The projected potential is almost identical to that of regular graphene (Fig. 1b), and the expected contrast difference between 'neutral' C and N atoms in the HRTEM simulation is less than 0.1% (Fig. 1c).

The situation is different if we include the charge redistribution due to chemical bonds for this configuration. Figure 1d shows a model of the N substitution in graphene along with the changes in the electronic charge density due to the chemical bonds. As discussed above, we highlight these changes by showing the difference between the DFT and IAM result. In addition, we have removed the periodic components of the graphene lattice from this difference image (see Supplementary Information for the unfiltered images). Remarkably, the strongest change in the charge density is around the three carbon atoms next to the nitrogen substitution, rather than on the N atom itself. The reduced electron charge density around the nitrogen atom leads to a reduced screening of the core potentials, and to a spatially extended signal in the projected potential. The corresponding DFT-based projected potential (with periodic components removed, and bandwidth-limited to approximately our experimental resolution (about 1.8 Å)) is shown in Fig. 1e: here, we see a spatially extended dark contrast, with a diameter of approximately two times the C–N bond (red dashed circle in Fig. 1e). We emphasize that the

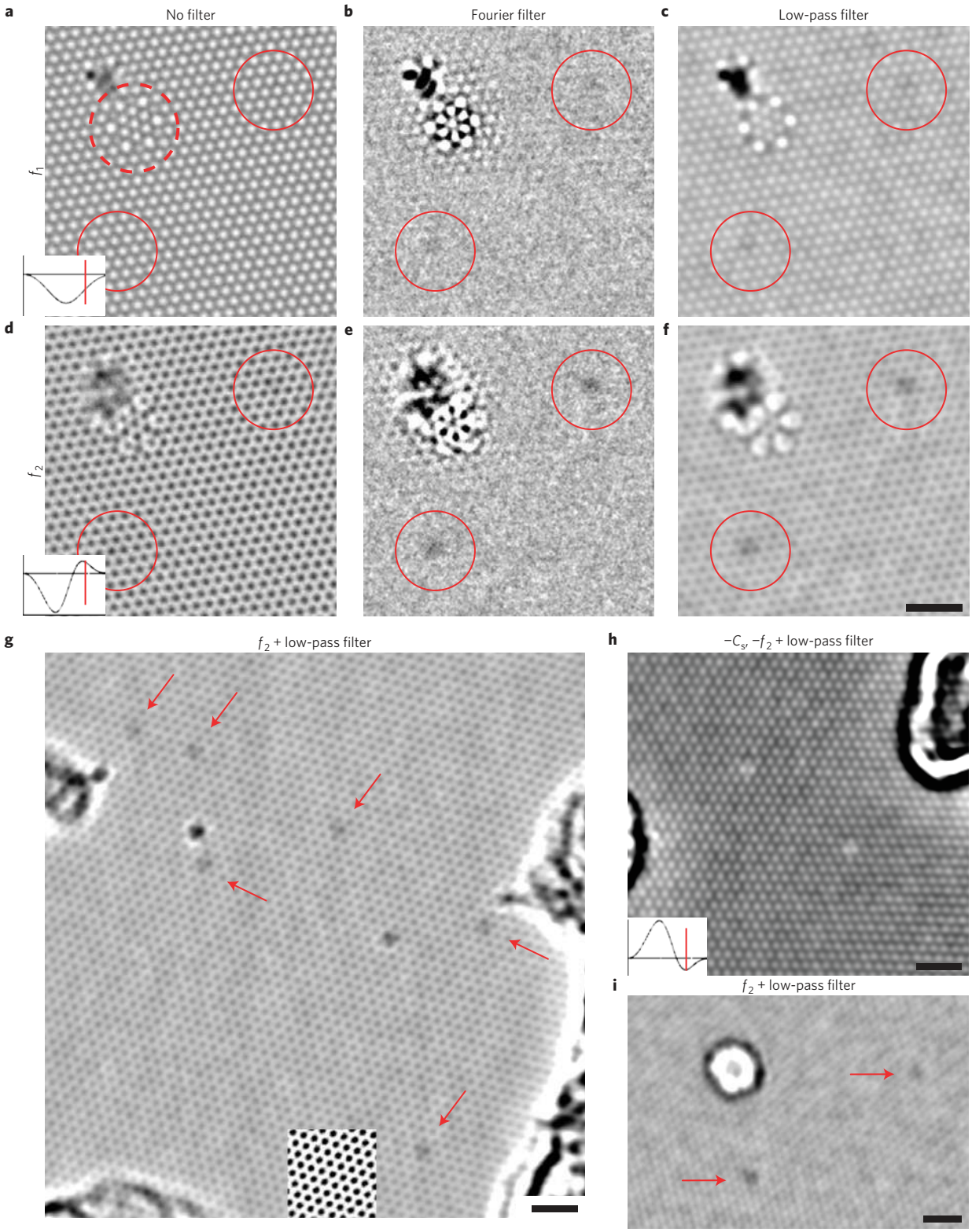

Figure 2 | Nitrogen dopants in graphene. Imaging conditions and filters in **a**–**f** are the same as in Fig. 1c,f. The red lines in the CTF plots (insets in **a**,**d**,**h**) indicate the 2.13 Å graphene lattice spacing. **a**–**c**, Scherzer defocus images. The dark contrast can be directly interpreted as atomic structure. However, the nitrogen substitution defects are not significantly above the noise (red circles). **d**–**f**, Larger defocus images (f_2) of the same area as shown in **a**–**c**. The nitrogen defects are clearly detected as a smooth dark contrast (in any case, a filter (**e**,**f**) is needed to discern the N dopants against the much stronger signal of the single layer graphene lattice). The extended defect (red dashed line in **a**) allows us to compare the same atomic position in both focus values. **g**, Image from a larger area, showing six nitrogen substitution defects marked by red arrows. The inset shows an unfiltered section of the image on the same contrast scale. **h**, Image of two nitrogen substitutions obtained with a reversed CTF (negative spherical aberration $-C_S$, positive defocus $-f_2$), showing the substitution positions as white areas. **i**, Irradiation-induced nitrogen substitutions (arrows, see text). The strong feature on the upper left is a beam-induced hole. All scale bars are 1 nm.

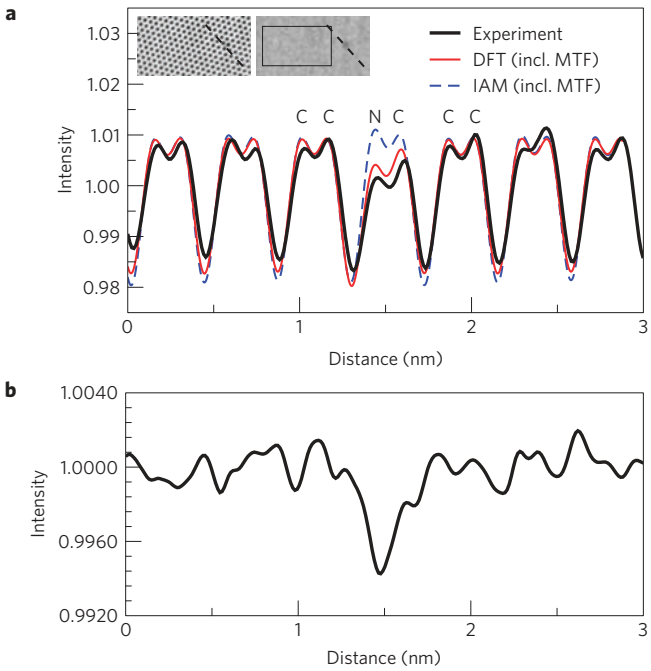

Figure 3 | Analysis of the nitrogen substitution defect. a, Comparison between experiment and simulations based on IAM and DFT potentials for defocus value f_2. MTF: modulation transfer function. Inset: The image and profile, and the Fourier-filtered image (graphene lattice removed). The noise level is measured as the standard deviation in a featureless region of the filtered image, close to the defect (black rectangle). A standard deviation of 0.0008 is found in this example. **b**, Line profile with the periodic components removed. The intensity dip at the nitrogen defect is seven times stronger than the standard deviation, and thus clearly above the noise.

signal due to bonding electrons here is not a point feature, as would be expected for a localized charge, an ad-atom or a heavier substitution atom. Hence, we can confirm from the experiment a charge redistribution over the nearest-neighbour atoms of a substitutional impurity, as shown below.

Indeed, the mostly lower-frequency components in the projected potential of the nitrogen substitution defect provide an additional complication to aberration-corrected HRTEM imaging of this defect. If we tune the spherical aberration and defocus so as to obtain a single pass-band in the contrast transfer function (CTF), the microscope acts as a high-pass filter and the defect is difficult to detect (about 0.3% contrast in a narrow point). This case is shown as 'defocus f_1' in our images. Under these conditions, dark contrast can be directly interpreted in terms of the atomic structure; however, the nitrogen substitution cannot be distinguished from the carbon atoms (even at our very low noise levels). Using a larger defocus (f_2), the CTF (Fig. 1c,f) shows oscillations but includes more of the lower spatial frequencies. Now, the nitrogen defect can be detected, yielding a stronger (about 0.6%) and also wider dark contrast. In any case, the nitrogen positions are most clearly visible when the graphene lattice is removed by a Fourier filter, or suppressed by a Gaussian low-pass filter. It must be emphasized that these filters are used only to find and highlight the nitrogen defects in the experimental data, as otherwise the small perturbation to the regular graphene lattice is difficult to see by eye. The comparison between simulation and experiment, which provides the direct experimental verification of the DFT-based charge densities, does not require any filters (Fig. 3a, discussed further below).

Experimentally, we identify single-layer graphene areas in the nitrogen-doped, chemical vapour deposition (CVD)-grown graphene sheets by an electron diffraction analysis[37,38]. We record long image sequences, >30 exposures with a pixel size of 0.2 Å and about 10^4 counts per pixel, for each value of defocus. Importantly, the graphene structure and defects of interest remain stable throughout the long exposure and associated high dose, which is a prerequisite to obtain the very high signal-to-noise ratio. Then, a drift-compensated average of 30–40 exposures is used. As predicted by the DFT model, the nitrogen substitutions exhibit a weak dark contrast in the larger defocus (f_2) images, but disappear below the noise as the focus is set to the Scherzer defocus conditions (f_1). As described above, this focus dependence confirms the mostly lower-frequency contribution in the projected potential for this defect.

Figure 2g–i shows additional images of N-doped graphene, with Fig. 2g being a larger area view of a CVD-grown sample. Figure 2h shows two nitrogen substitutions imaged with reversed contrast transfer (negative C_S, positive defocus $-f_2$), where the substitution atoms are revealed as weak white spots. Figure 2i shows an alternative way to fabricate atomic substitutions in graphene: here, an undoped graphene sample was briefly exposed to higher energy electrons (300 kV, about $10^7\,e^-\,nm^{-2}$), and subsequently imaged at 80 kV to prevent further damage. After such a treatment, we also find nitrogen substitution defects. A likely mechanism is a substitution of beam-generated vacancies by nitrogen atoms from the environment. However, we note that also a variety of other defects are generated by this approach.

A quantitative comparison between the simulation and experiment is shown in Fig. 3. For this comparison, the modulation transfer function of the CCD (charge-coupled device) camera was measured and applied to the simulated images, following the procedure of ref. 39. In addition, a small (0.7 Å full-width at half-maximum) Gaussian blur was applied to both, unfiltered experimental data and simulation, to reduce the pixel noise in the highly oversampled experimental data. As can be seen in Fig. 3a, an excellent confirmation of the DFT-based simulation is obtained. Hence, our experiment confirms the DFT-based charge density and the corresponding electrostatic potential, whereas the IAM clearly disagrees with the experimental data.

We now turn to the calculations and measurements for the single-layer hBN. The conventional IAM TEM simulation is shown in Fig. 4a,b, and Fig. 4c,d shows the TEM image simulation for the DFT-based electrostatic potentials for the bonded configuration. In this partially ionic compound, charge is accumulated on the nitrogen site[28]. Hence, one would expect a stronger screening of the N core potential, and thus a reduced contrast for this element. Nevertheless, the quantitative simulation result from the DFT calculation (Fig. 4e) shows a peculiar coincidence: the charge transfer happens to be such that the contrast difference between the B and N site, as expected from the neutral-atom (IAM) simulation, is almost exactly cancelled. In other words, single-layer hBN looks identical to graphene in HRTEM images (at our conditions) because of its ionic character. Thus, we can confirm the DFT prediction and verify the ionicity of single-layer hBN from HRTEM images, but we cannot assign the B and N sublattices.

For the experimental case, the separation of intrinsic contrast (that is, that of the sample) and effects of optical aberrations (from the microscope) is very important, and discussed in more detail in the Supplementary Information. The effects can be separated by the comparison between single-layer and bilayer hBN. For a bilayer, a symmetric profile is expected owing to the symmetry of the projected structure (B is above N). Hence, any asymmetry in the bilayer profile represents only the residual electron optical aberrations. Assuming identical imaging conditions for all points of the sample, the comparison between a single-layer and bilayer region would show the 'intrinsic' contrast difference in the monolayer, if present (however, the assumption of identical imaging conditions in separated areas is not always justified—

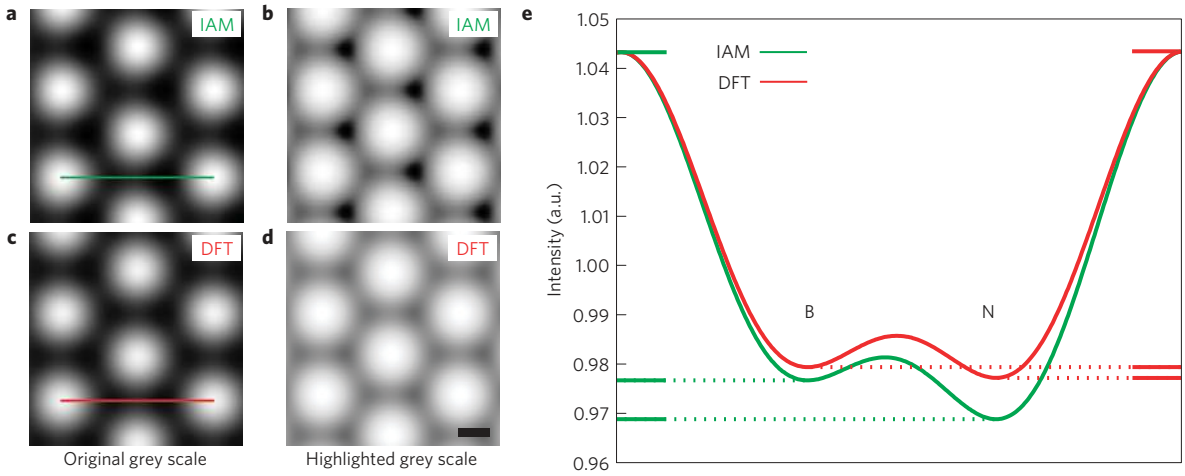

Figure 4 | Simulated TEM images for hBN. a,**b**, Conventional, IAM TEM image simulation for single-layer hBN. **c**,**d**, TEM simulation using potentials from the all-electron DFT simulation. **e**, Intensity profile plots for the two simulations. The scale bar in **d** is 1 Å.

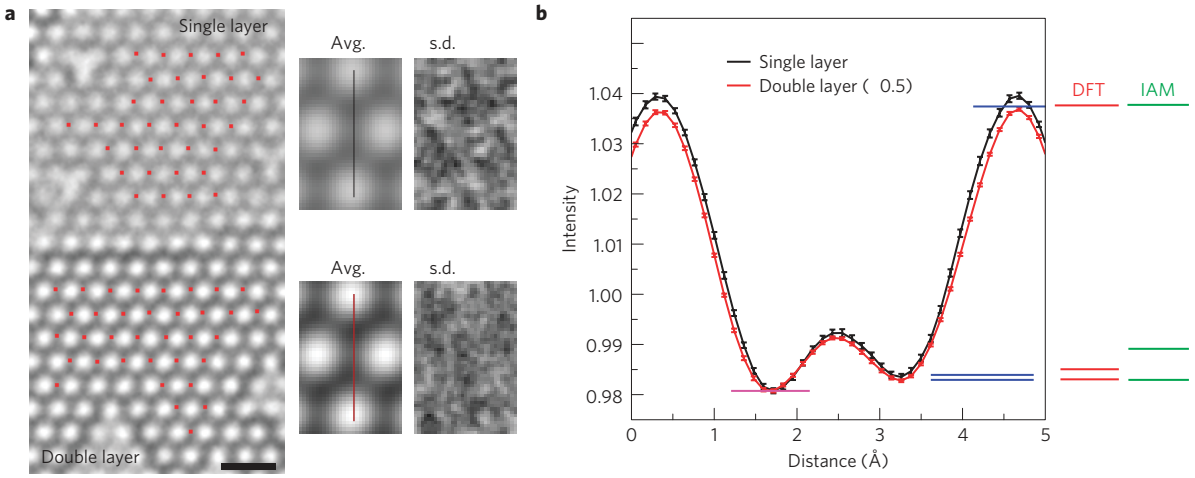

Figure 5 | Experimental data for hBN. a, Image of single- and bi-layer hBN (scale bar is 5 Å). The unit cells indicated by the red dots were chosen for analysis (away from defects and edges); shown here is the average and standard deviation. **b**, Intensity profiles from the single- and double-layer average (standard deviation as error bars). The contrast of the double layer was numerically reduced by a factor of 2 for comparison. The intensity minimum on the left sublattice was shifted to the same value (pink line), and then the intensity on the right sublattice is compared (blue lines). The contrast difference expected from IAM and DFT model is indicated.

we discuss this point in the Supplementary Information). The experimental result is shown in Fig. 5. Figure 5a shows the direct image (average of 21 exposures), with 35 selected unit cells indicated in both areas, and their average and standard deviation. Figure 5b shows the corresponding intensity profiles. The error bar represents the standard deviation as the mean deviation of individual unit cells from their average. With a very high precision, the intensity profiles of the single-layer and double-layer hBN regions are identical. We estimate an experimental error of 3% relative contrast difference between B and N (relative here means compared with the total modulation, that is, the contrast difference between the hole in the hexagon and the atom sites), on the basis of comparisons of separated regions with the same thickness. This means that the ionic character of single-layer hBN is confirmed, and that the charge distribution in the DFT result is correct within our experimental errors. The neutral-atom (IAM) charge distribution, which predicts a relative difference of 10%, can be ruled out.

As we have shown, details of the electronic configuration can be detected in TEM images with a high signal-to-noise ratio obtained under carefully controlled conditions. One key ingredient is the fabrication of samples with precisely defined geometries[23], and a reduction of radiation damage to allow sufficiently high signal-to-noise ratios. Graphene and hBN are special because they are easy to prepare in such well-defined geometries, and maintain their crystalline surface configurations even under ambient conditions. On this basis, we can speculate what would be required to detect charge transfer in other systems. We note that much larger chemical shifts than detected here have been predicted for a variety of materials in refs 23,24, but could not be measured owing to artefacts of common TEM sample preparation methods. The obvious implication is that one would need new ways of sample preparation and transfer to the TEM, because the surfaces of many materials become amorphous already by exposure to ambient conditions. Moreover, the low-voltage electron beam seems to be important to avoid sample amorphization (including the sample surface) in the electron beam. The single-layer thickness of the sample, however, is most likely not a key requirement, as can be deduced from the earlier calculations[22–24].

In our examples, the experiments confirm the DFT-based potentials (and thereby the charge densities), which might not be too surprising given that these are relatively simple systems. Nevertheless, we successfully distinguish between two candidate

models for the charge distribution (IAM versus DFT) that differ only in the distribution of binding electrons. This is achieved for a non-periodic configuration, a single-atom point defect. It is therefore straightforward to see the potential case, where a charge distribution for a more complex configuration is not so easy to model, and then a HRTEM experiment may provide important guidance. We have demonstrated the case of a point defect, and calculations in ref. 22 indicate that charge transfer at an interface may also have similarly detectable effects. Finally, we note that electron holography experiments should in principle provide the same information as we show and discuss here, that is, information that is contained in the projected potentials.

At the same time our results also show that, in cases where small differences in elemental contrast are important, bonding effects have to be taken into account. For example, the contrast difference between the B and N sublattices in HRTEM images of hBN single layers is much smaller than expected from the IAM approximation, and the experiment confirms this prediction once the imaging conditions are sufficiently well controlled. Hence, the question of which element forms the stable mono-vacancies in hBN surfaces under TEM observation[29–31], remains unclear. For the case of N-doped graphene, one would expect from IAM simulations that a N substitution in graphene cannot be detected. It is exclusively the effect of binding electrons that makes it possible to find nitrogen substitutions in graphene. Nitrogen substitutions in graphene—possibly irradiation-induced—also provide an alternative explanation to the weak dark contrast observed in ref. 40 (nitrogen substitutions had been ruled out on the basis of IAM calculations with atomic configurations from the literature, whereas a DFT-based calculation provides a reasonable agreement). As another remarkable point, the contrast of the N defect is primarily due to a change in the electronic configuration on the neighbouring carbons, rather than on the nitrogen atom itself, and it is due to a higher moment (a dipole) in the charge density on these atoms. Hence, it is also not possible to model these effects by using modified scattering factors for partly ionized atoms.

We have shown that it is possible to obtain insights into the charge distribution in nanoscale samples and non-periodic defects from HRTEM measurements. For our examples of the nitrogen substitutions in graphene and hBN layers, we can assign experimentally observed contrast features to details in the simulated electron distribution. We can detect a single light substitution atom in graphene, which is possible only because of the electronic effect. In the case of hBN, the charge redistribution leads to a loss of the elemental contrast difference. Instead, the ionic character of the material is experimentally confirmed for the single layer. One key ingredient here is the extraordinary stability of the samples under the low-voltage electron beam, which allows us to obtain extremely high signal-to-noise ratios from long exposures. The precisely defined, ultrathin sample geometry enables a straightforward analysis. The DFT-based TEM image calculation is irreplaceable for the interpretation of experimental results in these materials, and can provide insights beyond the structural configurations.

Methods

Preparation of nitrogen-doped graphene membranes and BN monolayers. We prepared nitrogen-doped graphene membranes by following the CVD methods for graphene synthesis[41–43], with the addition of small amounts of ammonia as the nitrogen source[25] during the growth. We have used both the CVD growth on nickel substrates and on copper substrates, and in both cases the addition of ammonia into the reaction has led to nitrogen-doped graphene sheets. We transfer the CVD-grown graphene sheets to commercial TEM grids as described previously[43]. Single-layer hBN is prepared and imaged as described previously[29].

Transmission electron microscopy. TEM imaging is carried out using an image-side aberration-corrected Titan 80-300, operated at 80 kV. The extraction voltage is reduced to 2 kV to reduce the energy spread of the source. The spherical aberration is set to about 20 μm and a defocus of $f_1 = -9$ nm (Scherzer defocus) and $f_2 = -18$ nm (graphene lattice in the second extremum of the CTF) are used.

Image processing. Post-filtering of the images is used to simplify the location of N substitution defects in our experimental data. We use here a Fourier filter that removes the periodic components of the graphene lattice, or a simple Gaussian low-pass filter chosen so that the graphene lattice contrast is reduced to about 0.5% (in this case the N substitution and graphene lattice appear with similar contrast).

Image calculation. TEM image simulations for the bonded atomic configuration follow the procedure of ref. 23 with some modifications. In brief, a relaxed atomic configuration is obtained using the Vienna *Ab initio* Simulation Package DFT code[44], which is well suited to carry out large-scale geometry optimizations in graphene-like systems from first principles[45]. Then, the WIEN2k DFT code[46] is used to obtain the all-electron self-consistent electron density and corresponding electrostatic potentials for this configuration. The TEM image simulation is then based on projections of this electrostatic potential, and otherwise follows the approximations for a thin specimen as in Chapter 3 of ref. 33.

Received 7 June 2010; accepted 9 December 2010; published online 16 January 2011

References

1. Hohenberg, P. & Kohn, W. Inhomogeneous electron gas. *Phys. Rev.* **136,** B864–B871 (1964).
2. Kohn, W. & Sham, L. J. Self-consistent equations including exchange and correlation effects. *Phys. Rev.* **140,** A1133–A1138 (1965).
3. Coppens, P. & Stevens, E. D. Accurate X-ray diffraction and quantum chemistry: The study of charge density distributions. *Adv. Quant. Chem.* **10,** 1–35 (1977).
4. Koritsanszky, T. S. & Coppens, P. Chemical applications of X-ray charge-density analysis. *Chem. Rev.* **101,** 1583–1627 (2001).
5. Vainshtein, B. K. *Modern Crystallography* (Springer, 1964).
6. Zuo, J. M. Measurements of electron densities in solids: A real-space view of electronic structure and bonding in inorganic crystals. *Rep. Prog. Phys.* **67,** 2053–2103 (2004).
7. Wu, L., Zhu, Y. & Tafto, J. Test of first-principle calculations of charge transfer and electron–hole distribution in oxide superconductors by precise measurements of structure factors. *Phys. Rev. B* **59,** 6035–6038 (1999).
8. Shibata, S., Hirota, F. & Shioda, T. Molecular electron density from electron scattering. *J. Mol. Struct.* **485,** 1–11 (1999).
9. Zuo, J. M., Kim, M., O'Keefe, M. & Spence, J. C. H. Direct observation of *d*-orbital holes and Cu–Cu bonding in Cu_2O. *Nature* **401,** 49–52 (1999).
10. Wu, L. *et al.* Valence-electron distribution in MgB_2 by accurate diffraction measurements and first-principles calculations. *Phys. Rev. B* **69,** 064501 (2004).
11. Hamers, R. J., Tromp, R. M. & Demuth, J. E. Surface electronic structure of Si-111 7×7 resolved in real space. *Phys. Rev. Lett.* **56,** 1972–1975 (1986).
12. Browning, N. D., Chisholm, M. F. & Pennycook, S. J. Atomic-resolution chemical analysis using a scanning transmission electron microscope. *Nature* **366,** 143–146 (1993).
13. Muller, D. A., Tzou, Y., Raj, R. & Silcox, J. Mapping sp_2 and sp_3 states of carbon at sub-nanometre spatial resolution. *Nature* **366,** 725–727 (1993).
14. Batson, P. E. Simultaneous stem imaging and electron energy-loss spectroscopy with atomic-column sensitivity. *Nature* **366,** 727–728 (1993.).
15. Muller, D. A. *et al.* Atomic-scale chemical imaging of composition and bonding by aberration-corrected microscopy. *Science* **319,** 1073–1076 (2008).
16. Gross, L., Mohn, F., Moll, M., Liljeroth, P. & Meyer, G. The chemical structure of a molecule resolved by atomic force microscopy. *Science* **325,** 1110–1114 (2009).
17. Weiss, C., Wagner, C., Temirov, R. & Tautz, F. S. Direct imaging of intermolecular bonds in scanning tunneling microscopy. *J. Am. Chem. Soc.* **132,** 11864–11865 (2010).
18. Wolf, E. L. *Principles of Electron Tunneling Spectroscopy* (Oxford Univ. Press, 1989).
19. Cox, G. *et al.* Scanning tunneling microscopy of crystal dislocations in gallium arsenide. *Phys. Rev. Lett.* **64,** 2402–2405 (1990).
20. Atamny, F., Spillecke, O. & Schlögl, R. On the STM imaging contrast of graphite: Towards a true atomic resolution. *Phys. Chem. Chem. Phys.* **1,** 4113–4118 (1999).
21. Gemming, T., Mobius, G., Exner, M., Ernst, F. & Ruehle, M. *Ab initio* HRTEM simulations of ionic crystals: A case study of sapphire. *J. Microsc.* **190,** 89–98 (1998).
22. Mogck, S., Kooi, B. J., De Hosson, J. Th. M. & Finnis, M. W. *Ab initio* transmission electron microscopy image simulations of coherent Ag–MgO interfaces. *Phys. Rev. B* **70,** 245427 (2004).
23. Deng, B. & Marks, L. D. Theoretical structure factors for selected oxides and their effects in high-resolution electron-microscope (HREM) images. *Acta Crystallogr. A* **62,** 208–216 (2006).
24. Deng, B., Marks, L. D. & Rondinelli, J. M. Charge defects glowing in the dark. *Ultramicroscopy* **107,** 374–381 (2007).

25. Wei, D. *et al.* Synthesis of n-doped graphene by chemical vapor deposition and its electrical properties. *Nano Lett.* **9,** 1752–1758 (2009).
26. Novoselov, K. S. *et al.* Electric field effect in atomically thin carbon films. *Science* **306,** 666–669 (2004).
27. Geim, A. K. & Novoselov, K. S. The rise of graphene. *Nature Mater.* **6,** 183–191 (2007).
28. Pauling, L. The structure and properties of graphite and boron nitride. *Proc. Natl Acad. Sci. USA* **56,** 1646–1652 (1966).
29. Meyer, J. C., Chuvilin, A., Algara-Siller, G., Biskupek, J. & Kaiser, U. Selective sputtering and atomic resolution imaging of atomically thin boron nitride membranes. *Nano Lett.* **9,** 2683–2689 (2009).
30. Jin, C., Lin, F., Suenaga, K. & Iijima, S. Fabrication of a freestanding boron nitride single layer and its defect assignments. *Phys. Rev. Lett.* **102,** 195505 (2009).
31. Alem, N. *et al.* Atomically thin hexagonal boron nitride probed by ultrahigh-resolution transmission electron microscopy. *Phys. Rev. B* **80,** 155425 (2009).
32. Krivanek, O. L. *et al.* Atom-by-atom structural and chemical analysis by annular dark-field electron microscopy. *Nature* **464,** 571–574 (2010).
33. Kirkland, E. J. *Advanced Computing in Electron Microscopy* (Plenum, 1998).
34. Doyle, P. A. & Turner, P. S. Relativistic Hartree–Fock X-ray and electron scattering factors. *Acta Crystallogr. A* **24,** 390–397 (1968).
35. Zhu, Z. H., Hatori, H., Wang, S. B. & Lu, G. Q. Insights into hydrogen atom adsorption on and the electrochemical properties of nitrogen-substituted carbon materials. *J. Phys. Chem. B* **109,** 16744–16749 (2005).
36. Lim, S. H., Li, R., Ji, W. & Lin, J. Effects of nitrogenation on single-walled carbon nanotubes within density functional theory. *Phys. Rev. B* **76,** 195406 (2007).
37. Meyer, J. C. *et al.* The structure of suspended graphene sheets. *Nature* **446,** 60–63 (2007).
38. Meyer, J. C. *et al.* On the roughness of single- and bi-layer graphene membranes. *Solid State Commun.* **143,** 101–109 (2007).
39. Thust, A. High-resolution transmission electron microscopy on an absolute contrast scale. *Phys. Rev. Lett.* **102,** 220810 (2009).
40. Meyer, J. C., Girit, C. O., Crommie, M. & Zettl, A. Imaging and dynamics of light atoms and molecules on graphene. *Nature* **454,** 319–322 (2008).
41. Kim, K. S. *et al.* Large-scale pattern growth of graphene films for stretchable transparent electrodes. *Nature* **457,** 706–710 (2009).
42. Li, X. *et al.* Large-area synthesis of high-quality and uniform graphene films on copper foils. *Science* **324,** 1312–1314 (2009).
43. Park, H. J., Meyer, J. C., Roth, S. & Skakalova, V. Growth and properties of few-layer graphene prepared by chemical vapor deposition. *Carbon* **48,** 1088–1094 (2010).
44. Kresse, G. & Furthmüller, J. Efficient iterative schemes for *ab initio* total-energy calculations using a plane-wave basis set. *Phys. Rev. B* **54,** 11169–11186 (1996).
45. Künzel, D., Markert, T., Groß, A. & Benoit, D. M. Bis(terpyridine)-based surface template structures on graphite: A force field and DFT study. *Phys. Chem. Chem. Phys.* **11,** 8867–8878 (2009).
46. Blaha, P., Schwarz, K., Madsen, G. K. H., Kvasnicka, D. & Luitz, J. *WIEN2k: An Augmented Plane Wave and Local Orbitals Program for Calculating Crystal Properties*. (Vienna Univ. Technology, 2001).

Acknowledgements

We gratefully acknowledge financial support by the German Research Foundation (DFG) and the Ministry of Science, Research and the Arts (MWK) of the state Baden-Württemberg within the Sub-Angstrom Low-Voltage Electron Microscopy project (SALVE) and by the DFG within research project SFB 569. T.I. acknowledges the JSPS Postdoctoral Fellowship for Research Abroad. G.A-S. acknowledges the support of CONACyT-DAAD scholarship.

Author contributions

J.C.M., A.C. and S.K. carried out TEM experiments. J.C.M., S.K. and A.C. analysed the data. S.K. carried out DFT calculations and TEM simulations based on WIEN2k. A.C. contributed to TEM simulations, discussions and analysis. H.J.P., V.S., S.R. and J.H.S. developed the synthesis of nitrogen-doped graphene. D.K. and A.G. carried out DFT calculations using the Vienna *Ab initio* Simulation Package. G.A-S. contributed to TEM simulations. T.I. and U.S. made Auger spectroscopy measurements. U.K. supervised part of the work. J.C.M. conceived and designed the study and wrote the paper. S.K. and U.K. co-wrote the paper.

Additional information

The authors declare no competing financial interests. Supplementary information accompanies this paper on www.nature.com/naturematerials. Reprints and permissions information is available online at http://npg.nature.com/reprintsandpermissions. Correspondence and requests for materials should be addressed to J.C.M. or U.K.